ELSEVIER

Precision Engineering 23 (1999) 177–184

PRECISION
ENGINEERING

Precision cylindrical face grinding

Albert J. Shih[a,*], Nien L. Lee[b]

[a]*Department of Mechanical and Aerospace Engineering, North Carolina State University, Raleigh, NC 27695-7910, USA*
[b]*Cummins Technical Center, Cummins Engine Co., Columbus, IN 47202-3005, USA*

Received 21 August 1998; received in revised form 2 February 1999; accepted 2 February 1999

Abstract

The mathematical models and experimental validations of precision cylindrical face grinding using a narrow ring superabrasive wheel are presented. The high pressure seal in diesel engine fuel systems demands the μm-scale form tolerance specifications and has driven the development of precision face grinding using the superabrasive wheel. Two mathematical models were developed: one was applied to predict the convex or concave face profile and another was used to simulate the abrasive trajectories, which become the cross-hatch grinding marks on the ground face. Cylindrical face grinding experiments were conducted. Experimental measurements of face profile and abrasive trajectories were used to validate the theoretical results. For high-pressure sealing surfaces, the height of face profile and grinding trajectories were two critical characteristics for design and manufacturing. Two design tools, a linear approximate solution for the profile height and an atlas for grinding trajectories, were developed to assist the selection of process parameters for the machine setup. © 1999 Elsevier Science Inc. All rights reserved.

Keywords: Precision grinding; Cylindrical grinding; Face grinding

1. Introduction

The diesel engine emission regulations have driven the design of fuel systems to achieve high-injection pressure for better atomization of diesel fuel and lower exhaust emission. To maintain good sealing of high-pressure diesel fuel between two mating surfaces, the cylindrical grinding process is applied to generate the μm-scale precision faces. The area of high-pressure seal has increased considerably in the new diesel fuel systems. This design change and the stringent form tolerance specifications have made the face grinding using conventional wheels difficult to meet the cycle time and statistical process control requirements. Recent advancements in the precision face grinding using a ring superabrasive wheel have demonstrated advantages in achieving tighter form tolerances, better statistical process control, longer wheel life, and less over-all production cost.

In the set-up of cylindrical face grinding, the wheel spindle was slightly tilted to generate the μm-scale precision convex or concave form on the face. This study presented systematic modeling to analyze effects of different set-up parameters on the form of the ground face. The early development on vertical spindle surface grinding using conventional wheels has been summarized by Shaw [1]. More recently, applications were extended to the diamond cup wheel grinding of the parabolic and toroidal surface on ceramics for mirrors [2,3] and on single-point diamond turning and cup wheel grinding of optics and mechanical components [4]. For the design of high-pressure seal in diesel fuel systems, the μm-level profile height (distance between the highest and lowest point on the face, as illustrated later in Figs. 3 and 4) is one of the critical characteristics. A simple mathematical formula is derived in this study to estimate the height of ground face profile.

During grinding, the hard abrasive on the wheel cuts across the face and generates two sets of grinding trajectories. As shown later in Figs. 9 and 10, these abrasive trajectories may be seen as the cross-hatch pattern on the ground surface. The pattern of grinding trajectories is another important design parameter for the high-pressure sealing surface. Another mathematical model was developed to calculate and plot these abrasive trajectories. By varying the set-up parameters, an atlas of different abrasive trajectories was developed to help the process design. Cylindrical face grinding experiments were conducted to validate both models.

---

* Corresponding author. Tel.: +919-515-5260; fax: +919-515-7968.
E-mail address: ajshih@eos.ncsu.edu (A.L. Shih)

PII: S0141-6359(99)00008-2

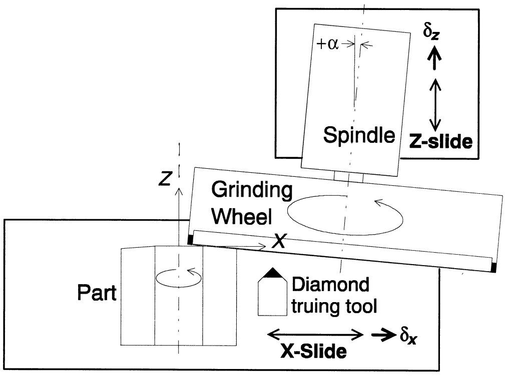

Fig. 1. Set-up of the cylindrical face grinding.

2. Mathematical Model for Form Grinding of Cylindrical Face

Fig. 1 shows the set-up of the cylindrical face grinding. A ring superabrasive wheel was used to generate a convex face on the rotating part, which was driven by a workhead. Two slides, X and Z, were used to carry the workhead and grinding wheel spindles, respectively. The directional vectors of the movements of X and Z slides were designated as $\boldsymbol{\delta}_X$ and $\boldsymbol{\delta}_Z$. $\boldsymbol{\delta}_X$ is perpendicular to $\boldsymbol{\delta}_Z$. The centerlines of the grinding wheel and workhead spindles intersect with each other. These two centerlines determine a plane. Both $\boldsymbol{\delta}_X$ and $\boldsymbol{\delta}_Z$ are parallel to this plane.

The diamond tool used to true the face grinding wheel is fixed on the X-slide. During truing, the feed was controlled by the sub-μm stepping movement of the Z-slide, and the traverse rate was determined by the speed of the X-slide. After truing, the X and Z slides positioned the grinding wheel to the configuration illustrated in Fig. 1 for grinding. The X-slide then remained stationary, while the Z-slide fed the wheel to grind the face on the rotating part. As shown in Fig. 2, two coordinate systems, XYZ and $R\theta Z$, were used to define the profile on the ground surface. The Z-axis coincided with the rotating axis of the workpiece and workhead. The X-axis was perpendicular to the Z-axis and parallel to $\boldsymbol{\delta}_X$. The X- and Z-axes were both located on the plane determined by centerlines of grinding and workhead spindles. By tilting the grinding wheel spindle a small angle α relative to the Z-axis, a convex or concave surface could be generated. If α is positive, as shown in Fig. 1, the ground surface is convex.

The grinding wheel is modeled as a ring of rotating abrasive. It removes the work material and generates a convex or concave form on the face of the rotating part. The part's inner and outer diameters are designated by r_i and r_o, respectively. The ring is offset by a distance s from the centerline of the part (Z-axis). The radius of the grinding wheel is r_g. In summary, there are five input parameters in this model: r_i, r_o, r_g, α, and s. The face surface is axisymmetric and independent of θ. The face profile in the RZ plane is sufficient to represent the surface of the ground face. In this paper, $Z = 0$ is set on the edge of the ground surface at $R = r_i$, as shown in Figs. 1 and 2 and later in Figs. 3 and 4. Also in this paper, the angle α is assumed small and $\cos \alpha \approx 1$.

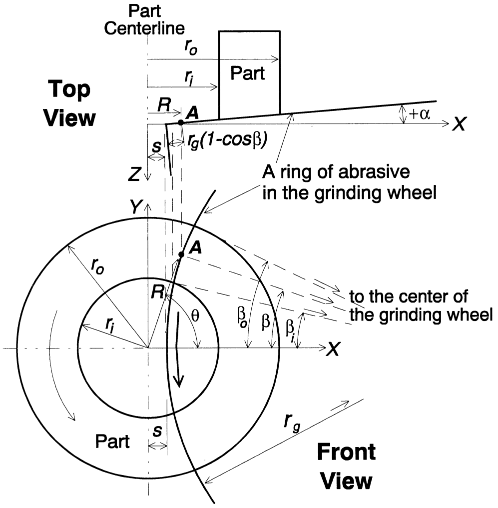

Fig. 2. The top and front views of XYZ and $R\theta Z$ coordinate systems to represent the part profile in cylindrical face grinding.

For the grinding wheel in Fig. 2, the inner and outer contact angles, β_i and β_o, between the wheel and part can be calculated as follows

$$\beta_i = \arccos\left(\frac{r_g^2 + (s + r_g)^2 - r_i^2}{2r_g(s + r_g)}\right) \tag{1}$$

$$\beta_o = \arccos\left(\frac{r_g^2 + (s + r_g)^2 - r_o^2}{2r_g(s + r_g)}\right) \tag{2}$$

A contact point A on the grinding wheel has an angle β referenced from the X-axis and $\beta_i < \beta < \beta_o$. The X, Y, Z, and R coordinates of the point A are:

$$X = r_g(1 - \cos \beta) + s \tag{3}$$

$$Y = r_g \sin \beta \tag{4}$$

$$Z = r_g(\cos \beta - \cos \beta_i)\sin \alpha \tag{5}$$

$$R = \sqrt{X^2 + Y^2} \tag{6}$$

Given the five input parameters, β_i and β_o can be calculated. An abrasive on the rotating grinding wheel has the β varying from β_o to β_i. The X, Y, Z, and R coordinates of the contact point A can be calculated using Eqs. (3) to (5). The following section will validate this model by comparing the theoretical results against experimental measurements.

It is interesting to note that, if the offset $s = 0$, the ring of abrasive will generate a spherical surface on the workpiece with a radius equal to $r_g/\sin \alpha$.

3. Experimental Validation of the Face Profile

Two grinding experiments were set up on a UVA cylindrical grinding machine using a vitreous bond, 150 ANSI

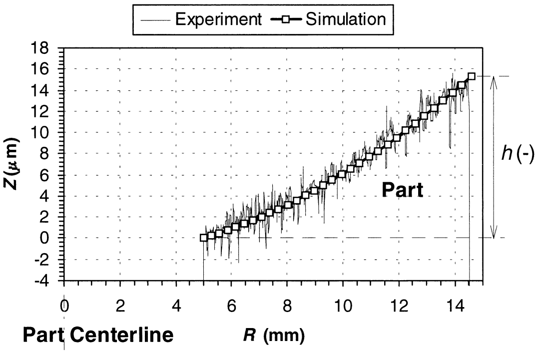

Fig. 3. Comparison of experimental and theoretical results of the concave face profile.

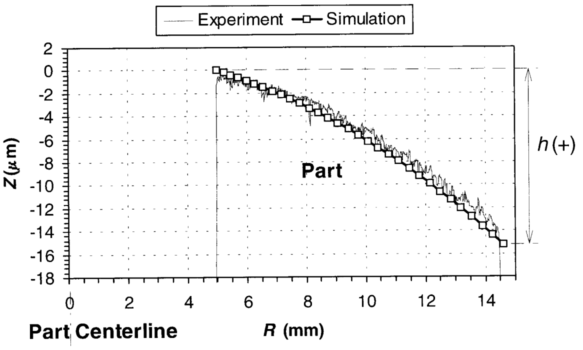

Fig. 4. Comparison of experimental and theoretical results of the convex face profile.

grit size ring CBN wheel. The work material was hardened ANSI 52100 steel. Several plunge grinding operations were used to generate a precisely ground surface for measurements. The depth of material removal in the final plunge grinding was limited to only 10 to 15 μm to minimize the error created because of machine deflection. After grinding, the face profile was measured in the radial direction using a Taylor Hobson Form Talysurf measurement machine.

3.1. Example 1. Concave Face Surface

The five set-up parameters are: $r_g = 147.1$ mm, $r_i = 5.0$ mm, $r_o = 14.6$ mm, $\alpha = -1.30°$ and $s = 4.0$ mm. Fig. 3 shows the comparison of the measured face profile against theoretical results. These two sets of data match each other very well and validate the proposed mathematical model.

3.2. Example 2. Convex Face Surface

Another test was conducted at $\alpha = +1.44°$ to generate the convex face. The other four parameters remain the same as in *Example 1*. Fig. 4 compares the theoretical and experiment profiles. It also validates the mathematical model.

4. Design of Process Parameters for Face Profile Height

For the high-pressure seal surface, one of the key tolerance specifications is the profile height h. As illustrated in Figs. 3 and 4, the definition of h is the Z-coordinate of the profile at $R = r_i$ minus the Z-coordinate of the profile at $R = r_o$. From Eq. (5),

$$h = r_g(\cos \beta_i - \cos \beta_o)\sin \alpha; \tag{7}$$

Substituting Eqs. (1) and (2) into Eq. (7) [Eq. (8)]

$$h = \frac{\sin \alpha (r_o^2 - r_i^2)}{2(s + r_g)} \tag{8}$$

Eq. (8) shows that the value of h can be increased by either increasing α and r_o or decreasing r_i, s, and r_g.

If the size of grinding wheel is much bigger than $s(r_g \gg s)$, and α is a small angle; that is, $\sin \alpha \approx \alpha$. The approximation solution h is

$$h \approx \frac{(r_o^2 - r_i^2)}{2r_g} \alpha \tag{9}$$

In practical shop floor environment, Eq. (9) is a simple and useful formula to estimate the initial set up for α and to determine the amount of adjustment for α to achieve the desired h. When r_i, r_o, r_g, and s remain the same, h has a linear relationship with α in Eq. (9).

4.1. Example 3

To illustrate the effects of α and s on h, the r_i, r_o, and r_g in grinding experiments in *Examples 1* and *2* were used. Fig. 5 shows both the closed-form and approximation solutions for h at $s/r_i = 0$ and 1. When $s = 0$ ($s/r_i = 0$), the approximate solution is very close the closed-form solution. In this case, the only source of error is the α to $\sin \alpha$ approximation. When $s = 5$ ($s/r_i = 1$), because $r_g = 147.1$ mm is much larger than s, the error, as seen in Fig. 5, remains under 4%.

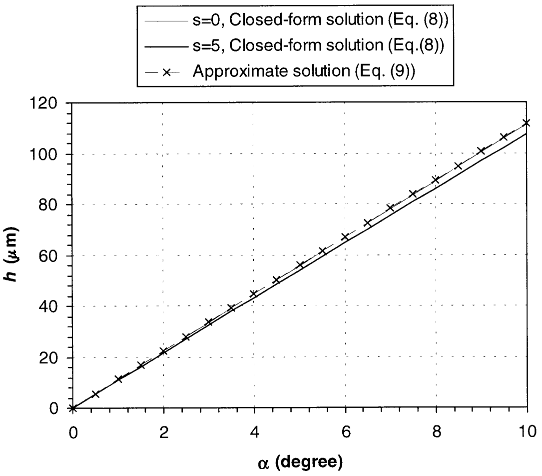

Fig. 5. The accuracy of approximation solution to estimate the profile height h.

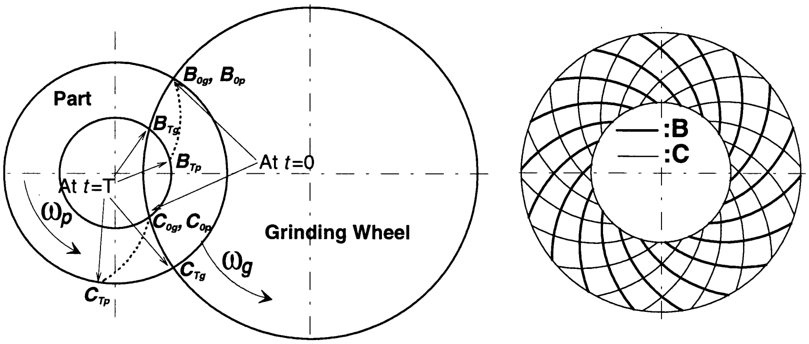

(a) (b)

Fig. 6. The mechanism generating two sets of grinding trajectories on the face, (a) the trajectories of abrasives *B* and *C* on the part and grinding wheel, (b) two sets of grinding marks on the ground surface.

5. Modeling the Abrasive Trajectories on the Ground Surface

As shown in Fig. 6(a), two sets of grinding marks are generated on the ground face. At time $t = 0$, a ring of abrasive is in contact with the part. An abrasive B_{0g} on the ring is in contact with the outside diameter and another abrasive C_{0g} is in contact with the inside diameter of the part. At time $t = T$, these two abrasives rotate from B_{0g} to B_{Tg} and from C_{0g} to C_{Tg}, respectively. Because the part is also rotating, abrasives *B* and *C* generate two curved grinding marks on the part from B_{0p} to B_{Tp} and from C_{0p} to C_{Tp}, respectively. Two sets of grinding trajectories are generated after grinding, as seen in Fig. 6(b). The abrasive rotates from B_{0p} to B_{Tp}, generating one set of trajectories, as shown by ***B*** in Fig. 6(b). The other set of trajectories ***C*** was created by the abrasive rotating from C_{0p} to C_{Tp}.

To completely define the grinding trajectories, a total of six parameters, r_i, r_o, r_g, s, ω_g and ω_p, are required. ω_g and ω_p are the angular velocity of the grinding wheel and part, respectively. ω_g and ω_p are positive in the c.c.w. direction. It is assumed that the tilt angle of the grinding wheel spindle α is small, and its effect on the abrasive is negligible.

To calculate the abrasive trajectory on the part, because both the part and grinding wheel are rotating, the transformation of relative position of the centers of the grinding wheel and part is necessary. As shown in Fig. 7(a), at time $t = 0$, the abrasive on the edge of the grinding wheel is in contact with the outside diameter of the part at B_0. The *XY*-coordinate system, with the origin located at the center of the part and *X*-axis pointing in the direction toward the center of the grinding wheel at $t = 0$, is defined. At time $t = \Delta T$, the effect of part rotation in the c.c.w. direction is modeled by rotating the center of grinding wheel an angle $\omega_p \Delta T$ in c.w. direction (opposite to the rotational direction of the part) relative to the center of the part, as shown in Fig. 7(b). In the meantime, the abrasive on the edge of the grinding wheel has rotated $\omega_g \Delta T$ in the c.c.w. direction to $B_{\Delta T}$. The *X*- and *Y*-coordinates of $B_{\Delta T}$ are $B_{\Delta T,X}$ and $B_{\Delta T,Y}$

$$B_{\Delta T,X} = (r_g + s)\cos(-\omega_p \Delta T) + r_g \cos(\theta_{0b} - \omega_p \Delta T + \omega_g \Delta T) \tag{10}$$

$$B_{\Delta T,Y} = (r_g + s)\sin(-\omega_p \Delta T) + r_g \sin(\theta_{0b} - \omega_p \Delta T + \omega_g \Delta T) \tag{11}$$

where

$$\theta_{0b} = \pi - \arccos\left(\frac{(r_g + s)^2 + r_g^2 - r_o^2)}{2(r_g + s)r_g}\right) \tag{12}$$

By incrementing the time, the points of *B* on the trajectory $B_{0p}B_{Tp}$ can be calculated using Eqs. (10)–(12). This trajectory ends at the time $T = [(\beta_o - \beta_i)/\omega_g]$, when the distance from *B* to the center of the part is less than r_i.

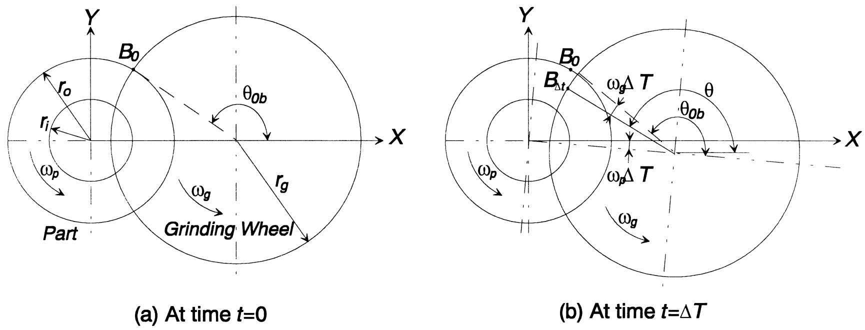

(a) At time *t*=0 (b) At time *t*=Δ*T*

Fig. 7. The mathematical model to calculate the trajectory of the abrasive **B** on the face.

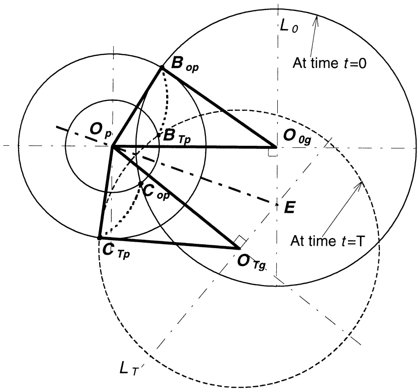

Fig. 8. The mirror reflection of the abrasive trajectories.

Similarly, the X- and Y-coordinates of the trajectory of abrasive C at time $t = \Delta T$ are $C_{\Delta T,X}$ and $C_{\Delta T,Y}$

$$C_{\Delta T,X} = (r_g + s)\cos(-\omega_p \Delta T) + r_g \cos(\theta_{0c} - \omega_p \Delta T + \omega_g \Delta T) \tag{13}$$

$$C_{\Delta T,Y} = (r_g + s)\sin(-\omega_p \Delta T) + r_g \sin(\theta_{0c} - \omega_p \Delta T + \omega_g \Delta T) \tag{14}$$

where

$$\theta_{0c} = \pi + \arccos\left(\frac{(r_g + s)^2 + r_g^2 - r_i^2)}{2(r_g + s)r_g}\right) \tag{15}$$

6. Proof of the Mirror Reflection of Trajectories $B_{0p}B_{Tp}$, and C_0C_{Tp}

Fig. 8 is used to prove that $B_{0p}B_{Tp}$, and $C_{0p}C_{Tp}$ are the mirror reflection across a line passing through the center of the part. At time $t = 0$, the abrasive ring intersects the outside and inside diameters of the part at B_{0p} and C_{0p}, respectively. At time $t = T$, the center of this ring is moved to O_{Tg}, $\angle O_{0g}O_pO_{Tg} = \omega_p$T. This ring, shown by the dashed circle, intersects the inside and outside diameters of the part at B_{Tp} and C_{Tp}, respectively. The two trajectories $B_{0p}B_{Tp}$, and $C_{0p}C_{Tp}$ are the mirror reflection across the line O_pE. E is located at the intersection of lines L_0 and L_T. L_0 is perpendicular to $O_{0g}O_p$ at O_{0g}, and L_T is perpendicular to $O_{Tg}O_p$ at O_{Tg}. To prove the mirror reflection of these two grinding trajectories, at first, we need to show that the distances from B_{0p} and C_{Tp} to O_pE are the same, and $B_{0p}C_{Tp}$ is perpendicular to O_pE. These two criteria can be proved by demonstrating that the two triangles $O_{0g}O_pE$ and $O_{Tg}O_pE$ and the other two triangles $O_{0g}O_pB_{0p}$ and $O_{Tg}O_pC_{Tp}$ are congruent to each other. Because $O_pO_{0g} = O_pO_{Tg} = r_g$, $\angle O_pO_{Tg}E = \angle O_pO_{0g}E = 90°$ and $O_{0g}E$ is the common side, triangles $O_pO_{0g}E$ and $O_pO_{Tg}E$ are congruent. Because all three pairs of corresponding sides of triangles $O_pO_{Tg}C_{Tp}$ and $O_pO_{0g}B_{0p}$ are equal ($O_pO_{Tg} = O_pO_{0g} = r_g + s$, $O_pC_{Tp} = O_pB_{0p} = r_o$ and $C_{Tp}O_{Tg} = B_{0p}O_{0g} = r_g$), these two triangles are also congruent. The congruence of these two sets of triangles conclude that B_{0p} and C_{Tp} are the mirror reflection across the line O_pE.

Following the same procedure, we can show that points B_{Tp} and C_{0p} are also the mirror reflection across the line O_pE. Moreover, at time $t = t_1$, $0 < t_1 <$ T, a point B_{t_1p} in the trajectory $B_{0p}B_{Tp}$ is the mirror reflection of the point C_{t_2p}, $t_2 =$ T $- t_1$, in the trajectory $C_{0p}C_{Tp}$.

7. Experimental Validation of Abrasive Trajectories

Grinding experiments were carried out at the same UVA grinding machine. Pictures of abrasive trajectories on the ground parts were used to compare to the theoretical results.

7.1. Example 4

In the grinding experiment, the six set-up parameters were $r_i = 5$ mm, $r_o = 14.6$ mm, $r_g = 147.1$ mm, $s = 0$ mm, $\omega_g = 1320$ rpm, and $\omega_p = 1800$ rpm. The picture of the ground face is illustrated in Fig. 9(a). These six experimental set-up parameters were used in the mathematical model [Eqs. (10) to (15)] to calculate two sets of grinding trajectories, as shown in Fig. 9(b). The good correlation between Figs. 9(a) and (b) validated the proposed model.

7.2. Example 5

All the process parameters remained the same as in *Example 4*, except the offset s is increased from 0.0 to 3.0 mm. The picture of ground face is shown in Fig. 10(a). The theoretical results are illustrated in Fig. 10(b). The increase in offset makes the two sets of grinding marks crossing each other. The good correlation between experiment and theoretical results validated the model.

8. Atlas for Grinding Trajectory Analysis and Design

An atlas with different abrasive trajectories on the ground face was created to assist the analysis and selection of process parameters. It is difficult to create a set of figures with six changing parameters. Therefore, some characteristics of the grinding trajectories had to be captured to find a way to reduce the number of parameters required to present different grinding trajectories. Also, if the new parameters are dimensionless, the inconvenience of unit conversion can be avoided. Extensive trial-and-error searches were conducted to find the three dimensionless parameters:

$\Omega = \dfrac{\omega_g}{\omega_p}$: dimensionless rotational speed;

$\Lambda = \dfrac{r_g}{r_o}$: dimensionless grinding wheel size; and

$\Phi = \dfrac{s}{r_i}$: dimensionless offset.

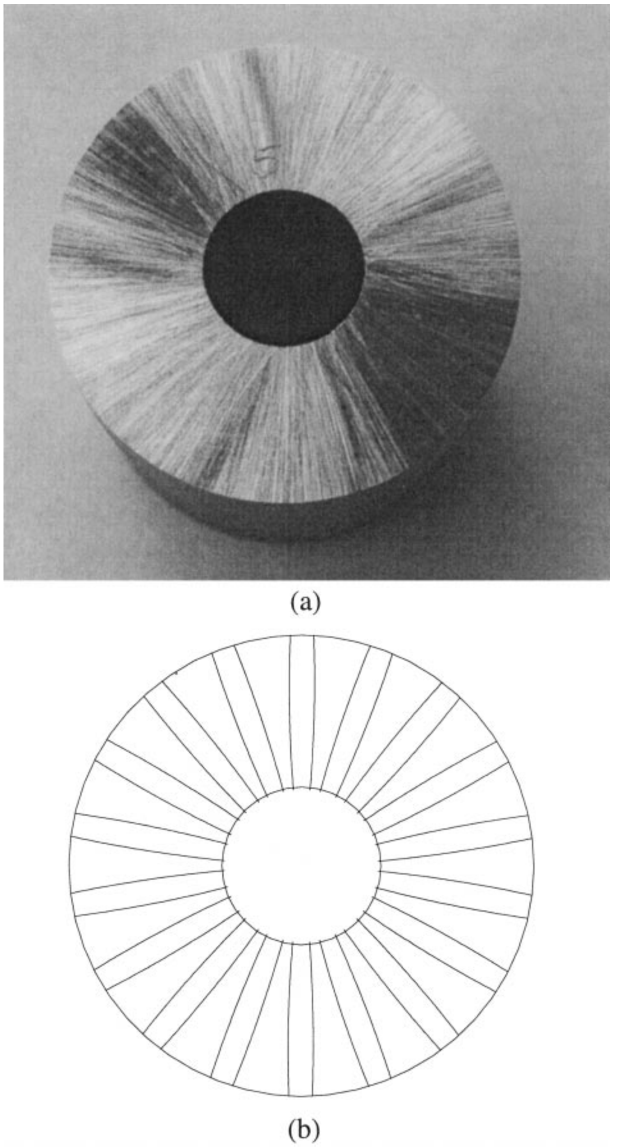

(a)

(b)

Fig. 9. (a) Picture of abrasive trajectories on the ground face; (b) theoretical results of abrasive trajectories.

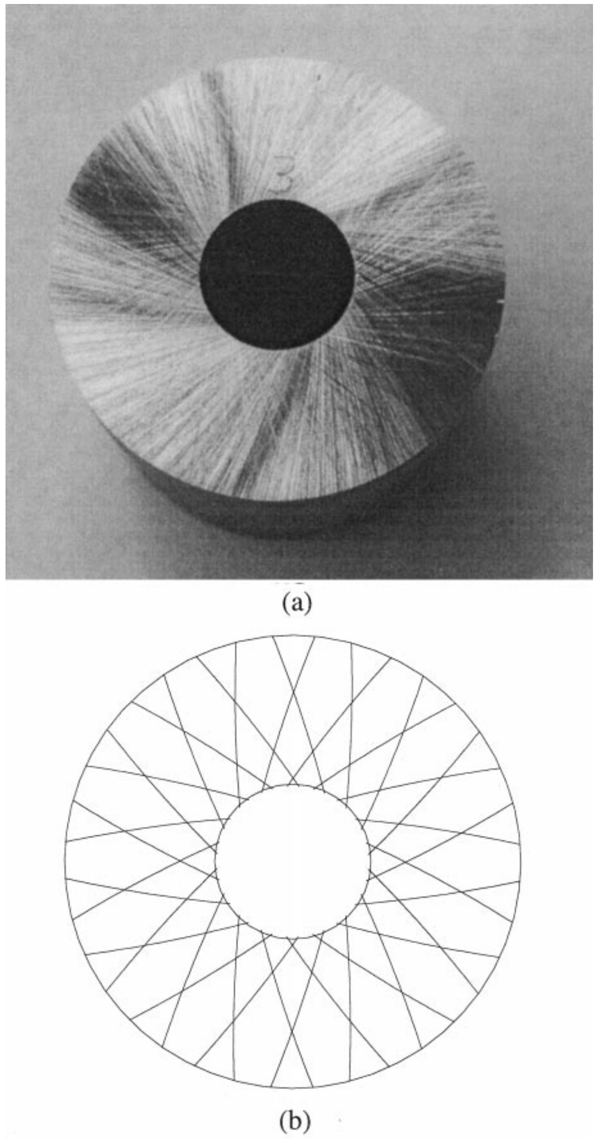

(a)

(b)

Fig. 10. (a) Picture of abrasive trajectories on the ground face; (b) theoretical results of abrasive trajectories.

Figs. 11–14 present an atlas of the abrasive trajectories based on these three parameters.

This set of three parameters is not the only set of dimensionless parameters that can be used to present the results. It is one of many ways to show the face-grinding trajectories in a systematic manner. To prove the proposed method is feasible, extensive tests were carried out. For example, the six input parameters were changed to find trajectories with the same Ω, Λ, and Φ. These trajectories must be identical to each other in the normalized scale. This paper did not provide rigorous mathematical proof that the use of these three dimensionless parameters could represent all abrasive trajectories. It is a task that needs further exploration.

The procedure to apply this atlas as a design and analysis tool is summarized in the following three steps:

- **Step 1:** Calculate the ratio of r_o/r_i and select the part outside boundary. All the parts shown in Figs. 11 to 14 have r_o four times bigger than $r_i(r_o/r_i = 4)$. Two dotted circles with radii equal to $2r_i$ and $3r_i$, respectively, are illustrated. These dotted circles are used to identify the outside boundary for different r_o/r_i ratios. For example, the part in the *Examples 1* and *2* has $r_i = 5.0$ mm, $r_o = 14.7$ mm, and $r_o/r_i \approx 3$. The first dotted circle from the outside diameter with $r_o/r_i = 3$ is used as the outside boundary for the grinding trajectories.
- **Step 2:** Calculate Φ and select a figure or two figures for interpretation. The four figures have $\Phi = 0.0$, 0.3, 0.6 and 0.9, respectively. If the calculated Φ matches one of the figures, it is the one to use. Otherwise, two figures with their Φ adjacent to the desired Φ are selected for interpolation.

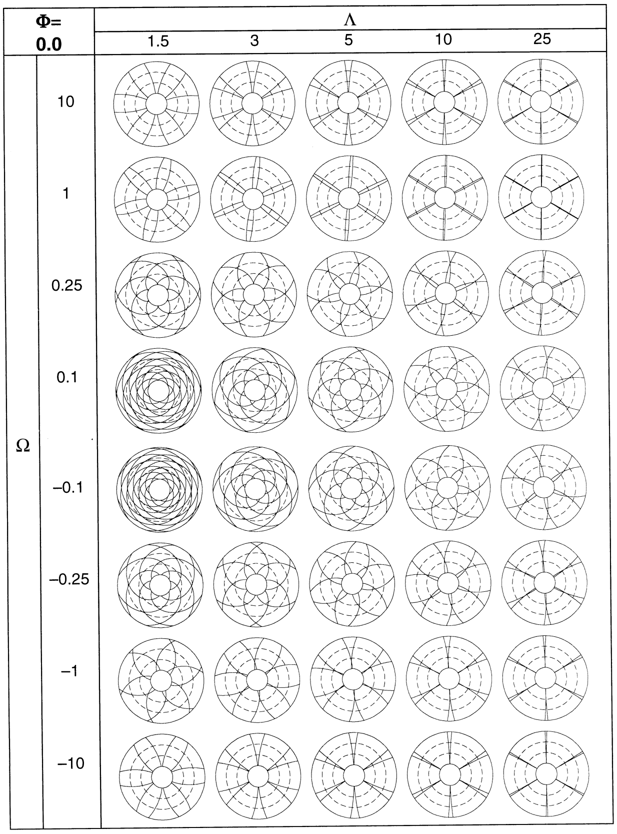

Fig. 11. Atlas of the face grinding trajectories at $\Phi = 0$.

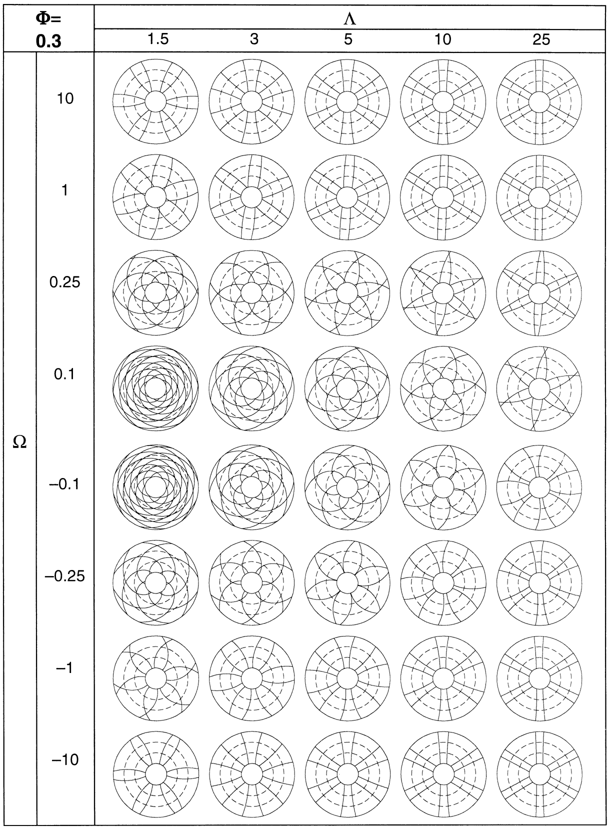

Fig. 12. Atlas of the face grinding trajectories at $\Phi = 0.3$.

- **Step 3:** Calculate Ω and Λ and select the appropriate rows and columns. Similar to Step 2, Ω and Λ are calculated to find the appropriate row and column, if the number matches. Otherwise, two rows or columns are selected to interpret the shape of trajectories.

The application of this procedure is illustrated in the next two examples.

8.1. Example 6

The process parameters in *Example 4* are used. The predicted grinding trajectories, based on the proposed procedure, must yield a shape close to that in Fig. 9. The three dimensionless parameters are $\Omega = 0.733$, $\Lambda = 10.07$, and $\Phi = 0$. First, the dotted circle of $r_o/r_i = 3$ is selected. Second, Fig. 11 is chosen, because $\Phi = 0$. Third, the column of $\Lambda = 10$ is used, and the two rows $\Omega = 0.25$ and 1.0 are selected for interpretation. The trajectories with $\Omega = 1.0$ are the closest to the actual $\Omega = 0.733$. The trajectories in $\Omega = 0.25$ indicate that the actual trajectories will be curved slightly. The predicted grinding trajectories match those in Fig. 9.

8.2. Example 7

The process parameters used in *Example 5* can be converted to $\Omega = 0.733$, $\Lambda = 10.07$ and $\Phi = 0.6$. The grinding trajectories must look similar to those in Fig. 10. The picture of $\Lambda = 10$, $\Omega = 1.0$, and $r_o/r_i = 3$ as the outside boundary in Fig. 13 was the best fit. Because $\Omega = 0.733$ instead of 1.0, the actual grinding trajectories were slightly curved, as seen in the picture of $\Omega = 0.25$ and $\Lambda = 10$. By comparing with the grinding trajectories in Fig. 10, the validity of this atlas was demonstrated.

9. Effects of Process Parameters on the Shape of Grinding Trajectories

From Figs. 10 to 14, the effects of each dimensionless parameters can be identified.

9.1. Effect of Ω

Ω represents the relative rotational speed of the grinding wheel versus the part. It can be positive or negative. Under the same Λ, Φ, and r_o/r_i, the positive and negative Ω with the same absolute value do not generate exactly the same grinding trajectories. The difference is more pronounced at the lower absolute value of Ω. When the absolute value of Ω is low, such as $\Omega = -0.1$ or 0.1, the part is rotating faster than the grinding wheel. The trajectories are curved more significantly. When $\Lambda = 1.5$ or 3.0 and $\Omega = -0.1$ or 0.1, the trajectories circle around the face several times.

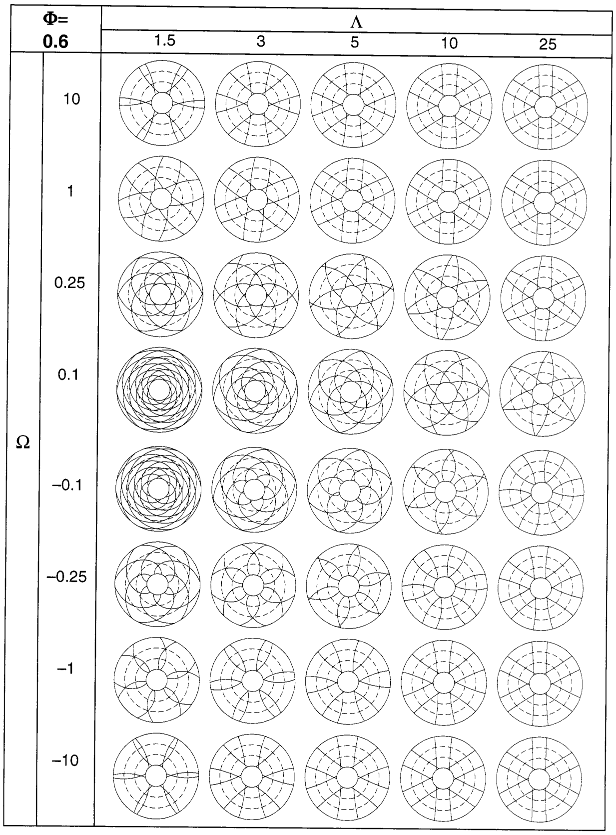

Fig. 13. Atlas of the face grinding trajectories at $\Phi = 0.6$.

9.2. Effect of Λ

Λ represents the size of the grinding wheel relative to the part. The high Λ means the grinding wheel is much bigger than the part. In this case, the trajectories appear more like the straight line.

9.3. Effect of Φ

The higher Φ stands for larger offset. It does not change the curvature of the trajectories significantly. Instead, higher offset shifts the trajectories away from the center of the part. When Φ is small, the trajectories has a trend to pass through the part center. By increasing Φ, the trajectories move away from the part center and tend to cross each other at a less acute angle. It could be seen by comparing the trajectories in *Examples 4* and *5* (Figs. 9 and 10), Φ was increased from 0.0 to 0.6, while all the other parameters remained the same.

9.4. Effect of r_o/r_i

Higher r_o/r_i means the abrasive stays on the face for a longer period of time. It increases the length of the trajectories on the face.

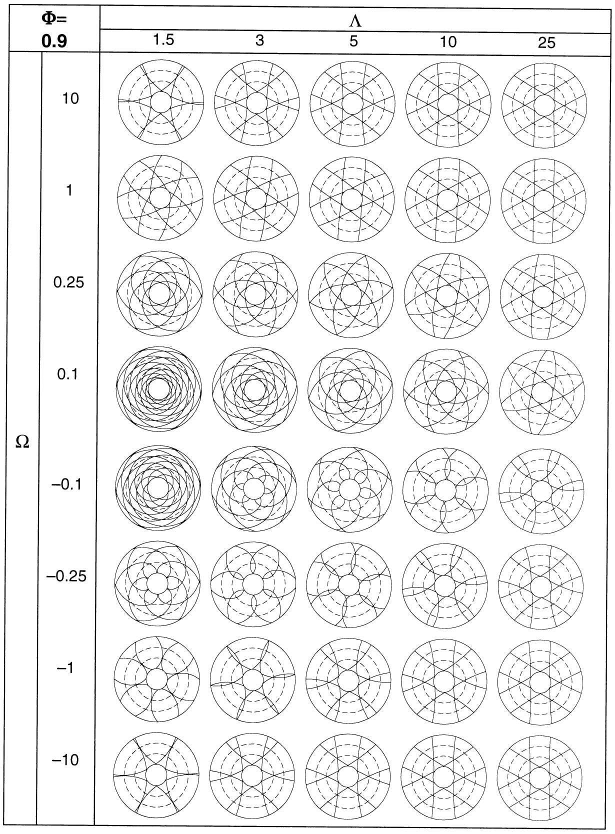

Fig. 14. Atlas of the face grinding trajectories at $\Phi = 0.9$.

10. Concluding Remarks

The profile and abrasive trajectories of the cylindrically ground face using the ring superabrasive grinding wheel are studied. Two mathematical models were developed to calculate the face profile and the abrasive trajectories. Both models were validated by comparing the theoretical results against experimental measurements. Two design tools were derived from the model. One was a linear approximate equation to predict the profile height *h*, and another was an atlas to help the selection of process parameters for the desired grinding trajectories. Examples of how to use these two tools were presented. The techniques developed in this study can be used for other types of face turning, lapping, or superfinishing processes to determine the tool trajectories and face profile.

References

[1] Shaw MC. Principles of Abrasive Processing. New York: Oxford University Press, 1996, Chap. 8.

[2] Zhong Z, Venkatesh VC. Generation of parabolic and toroidal surfaces on silicon and silicon-based compounds using diamond cup grinding wheels. Ann CIRP 1994;323–6.

[3] Zhong Z, Nakagawa T. Grinding of aspherical SiC mirrors. J Mat Proc Technol 1996;56:37–44.

[4] Dow TA, Fornaro R, Scattergood RC. Virtual Reality in Precision Manufacturing Processes, Office of Naval Research, 1997, Grant No. N00014-92-J-4099.